HOT CORROSION MECHANISM OF NiCr - 40 % Cr_3C_2 HIGH-VELOCITY OXY-FUEL THERMAL SPRAY COATINGS ON STAINLESS STEEL 304

Muhamad Waldi[1], Adi Wirawan[2], Eddy Agus Basuki[2],
Budi Prawara[3], Erie Martides[3], Endro Junianto[4]

[1]*Department of Metallurgical Engineering*
Faculty of Manufacturing Technology
Universitas Jenderal Achmad Yani
Bandung 40285, Indonesia, muhamad.waldi@lecture.unjani.ac.id (M.W.)
[2]*Department of Metallurgical Engineering*
Faculty of Mining and Petroleum
Engineering, Institut Teknologi Bandung
Bandung 40132, Indonesia, adi@lomatimine.gold (A.W.);
eddy.a.basuki@itb.ac.id (E.A.B),
[3]*Research Center for Advance Materials*
National Research and Innovation Agency (BRIN), South Tangerang 15314
Indonesia, budi029@brin.go.id (B.P.); erie001@brin.go.id (E.M.)
[4]*Research Center for Smart Mechatronics*
National Research and Innovation Agency (BRIN)
Bandung 40132, Indonesia, endr006@brin.go.id (E.J.)

Received 28 January 2025
Accepted 15 July 2025
DOI: 10.59957/jctm.v61.i1.2026.18

ABSTRACT

The hot corrosion characterization of High-Velocity Oxy-Fuel (HVOF) thermally sprayed coatings of 60 % $NiCr_{[37\,\mu m]}$ - 40 % Cr_3C_2 on stainless steel 304 substrate was analysed by exposure to molten salts Na_2SO_4 and NaCl of various mole percentages at a temperature of 750°C. The application of finer NiCr feedstock 37 μm has been effective to improve the quality of thermal spray coatings both in physical and mechanical properties. In this study, the NiCr based coatings is evaluated in the hot corrosion test to verify its reliability. XRD and SEM characterizations were applied to analyse compounds resulting from the hot corrosion process, the depth of pitting, oxide thickness, spalling, and decarburization. Results showed that the higher the mole percentage of salt NaCl, the thicker the oxide and the deeper the pitting formed on the coating surface, and that the oxide formed was Cr_2O_3 and NiO. Furthermore, decarburization of Cr_3C_2 was severe and formed due to hot corrosion on the specimens were classified as type II, in the other hand the decarburization was not detected on the surface of the specimen after the hot corrosion test. However, spalling was evident on every specimen.

Keywords: coating, HVOF, hot corrosion.

INTRODUCTION

The world population in 2024 was 8.2 billion people, and it is expected to reach 9.7 billion in the year 2050 [1]. It is predicted that the need for electricity will also rise by as much as 28 % in the year 2040 [2]. The most common power plant used today is the coal-fired power plant because it uses coal which is relatively cheap. The downside is that its combustion results in the greenhouse effect. Therefore, the efficiency of coal-fired power plants must be developed, and their electricity production increased using the same amount of fuel or less. Furthermore, to improve the efficiency of steam power plants, temperature and steam pressure

must be increased [3, 4]. Hence, reliable materials are needed to overcome high temperatures, oxidation, and hot corrosion [5]. One alternative is by means of coating deposition with feedstock 60 % $NiCr_{[37\ \mu m]}$ - 40 % Cr_3C_2 applied by HVOF on stainless steel 304 substrate. HVOF is a thermal spray coating (TSC) that takes place under conditions of high pressure and combustion temperatures. HVOF involves the heating of feedstock material to form melted or semi-melted droplets which are then propelled through a spray gun with a stream of pressurized gas toward the surface of the substrate to form a new surface structure, resulting in low porosity durability, and high density [6 - 9].

The feedstock for the top coat was 60 % $NiCr_{[37\ \mu m]}$ - 40 % Cr_3C_2 which strongly resists hot corrosion, prevents decarburization, and is highly durable. The bond coat consisted of Ni - 20 % Cr to provide a high level of adhesiveness between the top coat and substrate. Previous research regarding the characterization of HVOF thermal spray coating with a NiCr matrix composite has been reported in 2018 to 2024 [9 - 11]. Using these prior researches and ISO 17224 as references, an analysis was conducted on the results of exposure to concentration variations of salt solution (Na_2SO_4 and NaCl) towards the rates of hot corrosion of thermally sprayed coating 60 % $NiCr_{[37\ \mu m]}$ - 40 % Cr_3C_2 with deposited of Na_2SO_4 and NaCl salts at a constant temperature of 750°C. The temperature refers to the operation temperature of the ultra-supercritical pulverized coal-fired power plants, and consideration of over temperature risk that might be occurred during the operation of coal-fired power plants.

EXPERIMENTAL

Materials and coatings

The NiCr powder (Metco 43C-NS, manufactured by Oerlikon Metco) was deposited as a bond coat material. For the top coat, the NiCr feedstock went through the sieve shaking process to obtain a finer powder distribution size to 400 mesh (37 μm). For the reinforcement, the selected feedstock was Cr_3C_2 brand Woka 7102 with 45 μm size manufactured by Oerlikon Metco). The materials were blended at a total weight 1 kg so that the cermet formula was 60 % $NiCr_{[37\ \mu m]}$ - 40 % Cr_3C_2. Stainless steel 304 with a thickness of 3 mm used as substrate, the material has been used as boiler material of ultra-supercritical pulverized coal-fired power plants. Prior to TSC in the confined chamber, 4 cm x 5 cm stainless steel 304 was prepared and blasted by white aluminium oxide in range 600 - 800 mesh.

TSC was carried out using a Tecknotherm HVOF 2007 machine and a Hipojet-2700 spray gun. Table 1 describes the parameters of the HVOF process applied in this research. To free water molecules, the feedstock material was preheated in a furnace at a temperature of 70°C for 15 h and then fed into the feeder. The metallic bond coat was initially deposited on the substrate, followed by cermet top coating deposition. Thus, the coating configuration was 60 % $NiCr_{[37\ \mu m]}$ - 40 % Cr_3C_2. The as-coated result of 60 % $NiCr_{[37\ \mu m]}$ - 40 % Cr_3C_2 deposited has typically grayish, rough surface resulted from HVOF TSC, physical appearance of the surface can be obtained from the previous work [12].

Hot corrosion test

Specimens were cut with a slow-speed precise saw into 1 cm × 1 cm pieces. Next, a salt solution was made from Na_2SO_4 and NaCl diluted using distilled water to produce 0.7 M. Four types of salt solution were made with different composition (wt. %): 100/0, 66/33, 33/66 and 0/100. Specimens were exposed in the molten salt for 1 minute then dried to allow a salt layer to deposit on the surface of the specimen. A hot corrosion test was then done in the muffle furnace at a temperature of 750°C for 5, 10, 25, and 50 h. After the specified times, each specimen was removed and cooled at an ambient

Table 1. Parameter of HVOF thermal spray.

Parameter	Unit	Value
Air pressure	MPa	0.62
Pressure O_2	MPa	0.8
Pressure N_2	MPa	0.5
Pressure Propane	MPa	0.55
Flow rate O_2	L min^{-1}	271
Flow rate N_2	L min^{-1}	8
Flow rate Propane	L min^{-1}	62.4
Powder feeder rotation	rpm	5
Stand off distance	mm	200
Spray angle	°	90
Substrate preheating	°C	100

temperature. A codification of respective specimens and treatments can be seen on Table 2.

Characterization of the coating

To verify corrosion produced on the surface of the specimen in the hot corrosion test, an X-ray diffraction (XRD) characterization was conducted using a Rigaku SmartLab X-ray diffractometer. In addition, a scanning electron microscope (JEOL JSM-IT300LA) were used to observe the thickness of the oxide, depth of pitting, spalling, and element distribution after the test.

RESULTS AND DISCUSSION

Hot corrosion mechanism

Fig. 1 reveals an SEM micrograph of TSC deposition of 60%$NiCr_{[37\,\mu m]}$ - 40 %Cr_3C_2 coatings. The micrograph features splats, un-melted particles, porosities and oxides [12 - 14]. The configuration of the coating interfaced with the substrate is a bond coat with varying thicknesses across the section. It is also distinguished by a pearly structure rich in Ni and Cr.

An SEM micrograph on specimen 50B, 50C and 50D showed pitting on the surface due to hot corrosion type II. Pitting on each specimen can be seen in Fig. 2. Specimens treated with 66/33 and 33/66 salt solution were melted because they formed a eutectic phase, whereas specimens treated with 100 % Na_2SO_4 and 100 % NaCl were not melted. A binary diagram of NaCl-Na_2SO_4 can be seen in Fig. 3.

Pitting was evident on the specimen with 100 % NaCl treatment because when melted it reacted with Cr metal, resulting in a Na_2CrO_4 compound. This compound can form a eutectic with salt NaCl, hence lowering the melting point to 577°C. A Na_2CrO_4 compound reaction can be seen in Eq. (1) [16]. The data of Gibbs free energies of formation were obtained from [17, 18].

$$½Cr_{(s)} + O_{2(g)} + NaCl_{(aq)} = ½Na_2CrO_{4(s)} + ½Cl_{2(g)}; \quad \Delta G_{750}: -466.612 \text{ kJ mol}^{-1} \qquad (1)$$

Oxide can also react with NaCl salt and form Na_2CrO_4 (Eq. (2)). Hence the protective oxide layer Cr_2O_3 is decreased and non-protective oxide [19, 20]. The damaged protective oxide layer Cr_2O_3 causes intensive corrosion where chlorine was able to penetrate [20, 21].

$$Cr_2O_{3(s)} + 4NaCl_{(aq)} + 5/2O_{2(g)} = 2Na_2CrO_{4(s)} + 2Cl_{2(g)}; \quad \Delta G_{750}: 249.562 \text{ kJ mol}^{-1} \qquad (2)$$

Hot corrosion type II could not be determined in specimen 100% $NaSO_4$. Pitting was not visible in SEM micrograph 50A. However, Ni can form into $NiSO_4$ because NiO oxide reacts with SO_3; then NiSO will form a eutectic with Na_2SO_4, lowering the melting point of Na_2SO_4 to 671°C. Thus, because pitting was not visible on specimen 50A, the specimen exposed to molten salt 100 % Na_2SO_4 did not experiencing pitting due to hot corrosion type II, unlike specimens exposed to Na_2SO_4 and NaCl salts. When $NiSO_4$ was not formed and Na_2SO_4 had not melted, the salt did not have any significance effects as in the liquid state.

Table 2. Specimen codification of salt solution concentration and hot corrosion time variation.

Na_2SO_4/NaCl, wt. %	Time, h			
	5	10	25	50
100/0	5A	10A	25A	50A
66/33	5B	10B	25B	50B
33/66	5C	10C	25C	50C
0/100	5D	10D	25D	50D

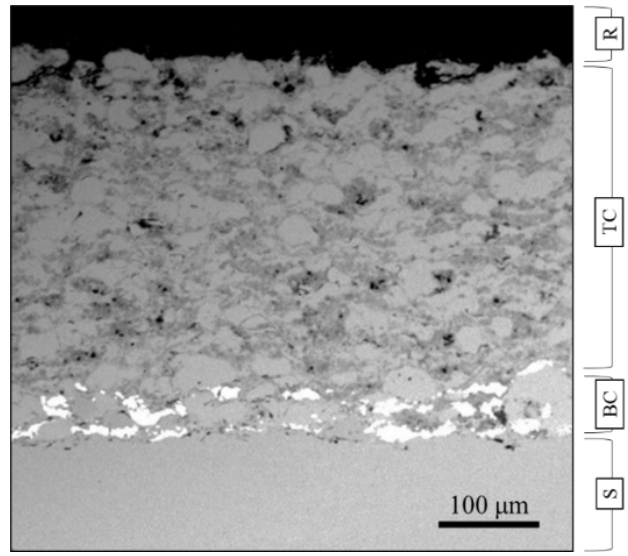

Fig. 1. SEM micrograph of HVOF TSC of 60% $NiCr_{[37\,\mu m]}$ - 40% Cr_3C_2 (S = substrate; BC = bond coat; TC = top coat; R = resin).

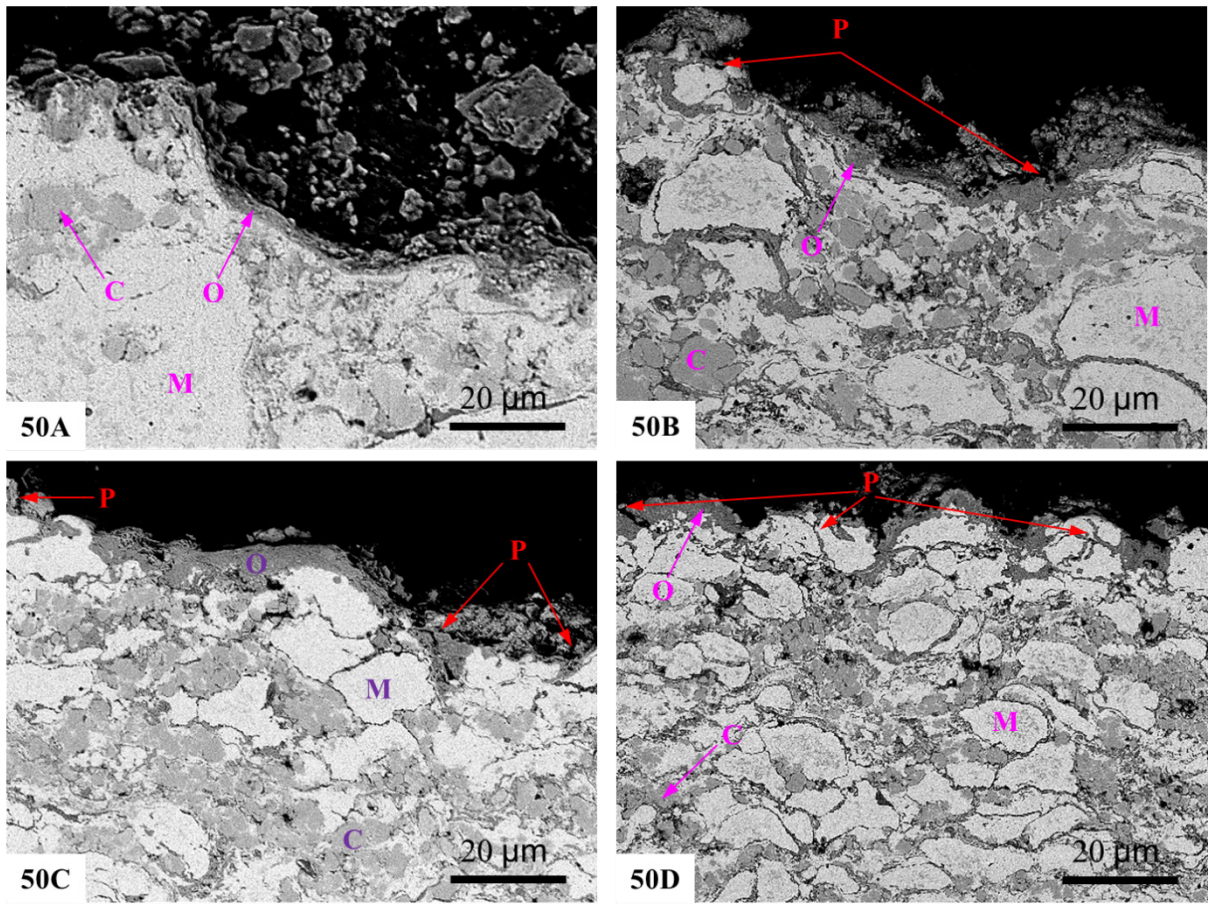

Fig. 2. SEM micrographs of specimens undergoing hot corrosion treatment for 50 h with varied mole of salts. Na_2SO_4/NaCl (50A. 100/0; 50B. 66/33; 50C. 33/66; 50D. 0/100). Remarks, P = pitting; M = matrix; C = carbide; O = oxide.

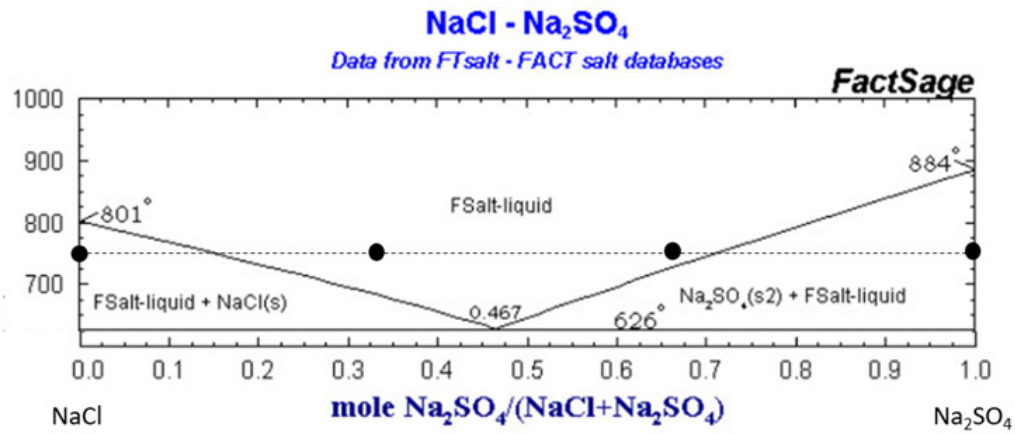

Fig. 3. Binary phase diagram of NaCl-Na_2SO_4 [15].

The hot corrosion mechanism starts with the formation of oxide Cr_2O_3 protecting the coating surface. The hot corrosion mechanism is divided into two phases: the initiation phase and propagation phase [22]. In the initiation phase, a reaction between melted salt and protective oxide occurs and causes protective oxide dissolve in the molten salt. Then, in the propagation phase, the corrosive species has a potential to deteriorate

the coatings below the oxide layer.

Oxide thickness

An X-ray diffractogram identified the existence of NiO and Cr_2O_3 oxides. A peak in Ni was also found to be significant, as depicted in the X-ray diffraction pattern of the 50 h hot corrosion test (Fig. 4). A significant peak of Ni was caused by the coating surface that was not thoroughly covered by an oxide layer, meaning that the higher the salt concentration, the less significant the Ni peak. An SEM micrograph of the 50D specimen shows oxide partially covering the coating surface, while some other parts of the surface were exposed (Fig. 5). 50D was the specimen which experienced the most severe from the hot corrosion.

It could be seen that the higher concentration of NaCl salt, the thicker the oxide resulted. The increase of oxide thickness paralleled the rise of NaCl formed

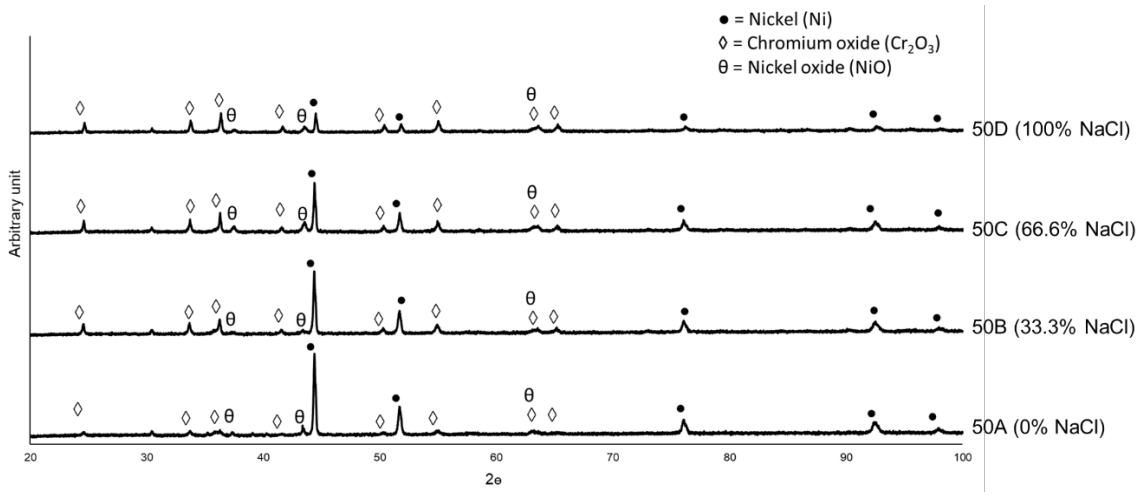

Fig. 4. X-ray diffraction pattern of specimens 50A, 50B, 50C, and 50D.

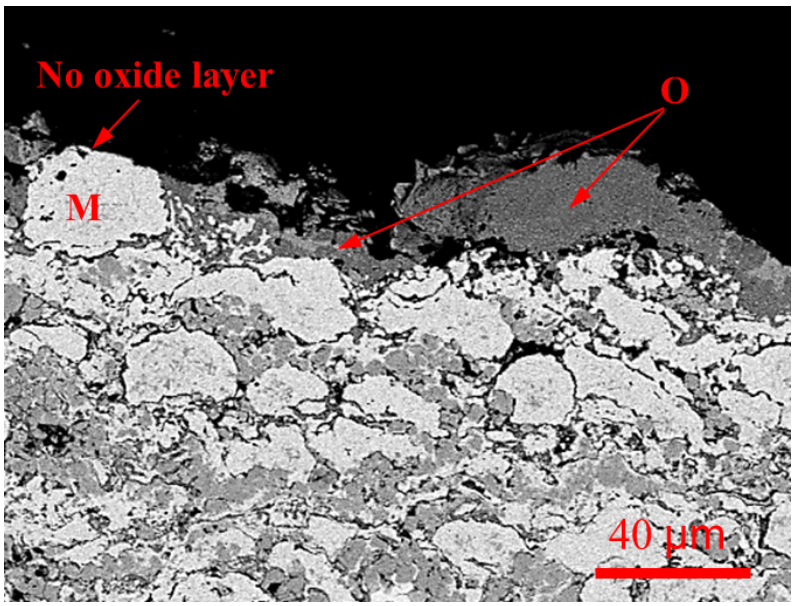

Fig. 5. Micrograph of specimen 50D shows parts that are covered by oxide layer and other parts that are not covered. Remarks, M = matrix; O = oxide.

from the gas Cl_2, which is a catalyst reaction from Cr oxidation [16].

Cr chlorination reaction [16], Eq. (3) and Eq. (4).

$Cr_{(s)} + Cl_{2(g)} = CrCl_{2(s)}$;

ΔG_{750}: -711.936 kJ mol^{-1} (3)

$2/3Cr_{(s)} + Cl_{2(g)} = 2/3CrCl_{3(s)}$;

ΔG_{750}: -648.075 kJ mol^{-1} (4)

Oxidation reaction of metal chloride [16], Eq. (5) and Eq. (6).

$4/3CrCl_{2(s)} + O_{2(g)} = 2/3Cr_2O_{3(s)} + 2Cl_{2(g)}$;

ΔG_{750}: -461.425 kJ mol^{-1} (5)

$4/3CrCl_3(s) + O_{2(g)} = 2/3Cr_2O_{3(g)} + 4/3Cl_{2(g)}$;

ΔG_{750}: -114.523 kJ mol^{-1} (6)

Cl_2 reacted with Cr to form metal chloride. The reaction was continuous where metal chloride reacted with oxygen forming oxide and the gas Cl_2, where the Cl_2 reacted with the metal Cr to form metal chloride and oxidized back again to cause the Cl_2 to behave as a catalyst in the metal Cr oxidation reaction [16]. Oxide Cr_2O_3 formed from the metal chloride oxidation was not protective because the oxide had pores [23]. Hence, the hot corrosion effect became severe.

The change of oxide thickness relative to the variation of mole percentage salts Na_2SO_4 and NaCl under hot corrosion treatment for 50 h is presented in Fig. 6a. Depth of pitting can be seen in Fig. 6b. Based on Fig. 6a and Fig. 6b, the increase of both oxide thickness and depth of pitting towards NaCl concentration is linear.

Oxidation of binary alloy and decarburizing

As shown in the micrograph of specimen 50D (Fig. 7), a thick oxide of Cr_2O_3 formed on the surface of the specimen, and the oxide NiO on top of the Cr_2O_3 layer. Based on the Ellingham diagram, Cr is more reactive than Ni; hence, Cr_2O_3 was formed earlier [24]. The Cr element was depleted during the formation of oxide Cr_2O_3; therefore, Cr concentrations dropped and Ni concentrations rose. Ni was able to form oxide NiO due to the rise in Ni concentration. The depletion of Cr is illustrated in Fig. 8. Transformation of the oxide Ni into NiO involved the migration of cation and electron out of the interface while oxidation was in progress, as illustrated in Fig. 9.

Growth of NiO oxide was faster than for Cr_2O_3. Based on previous research by Roy et al. in 2001, the thickness of Cr_2O_3 is lower than that of NiO oxide. However, this research resulted in the oxide Cr_2O_3 being thicker than NiO [25]. This was due to three matters: Firstly, the Cr concentration in carbide Cr_3C_2 was higher than 20 %; secondly, the carbide Cr_3C_2 experienced decarburization; and lastly, the gas Cl_2 was evident as the catalyst of metal Cr oxidation.

The XRD result showed no evidence of Cr_3C_2, Cr_7C_3, and $Cr_{23}C_6$ compounds. However, carbide Cr_3C_2 experienced severe decarburization. Metal Cr was oxidized by O_2 and formed Cr_2O_3 compound. Decarburization occurred due to high temperatures,

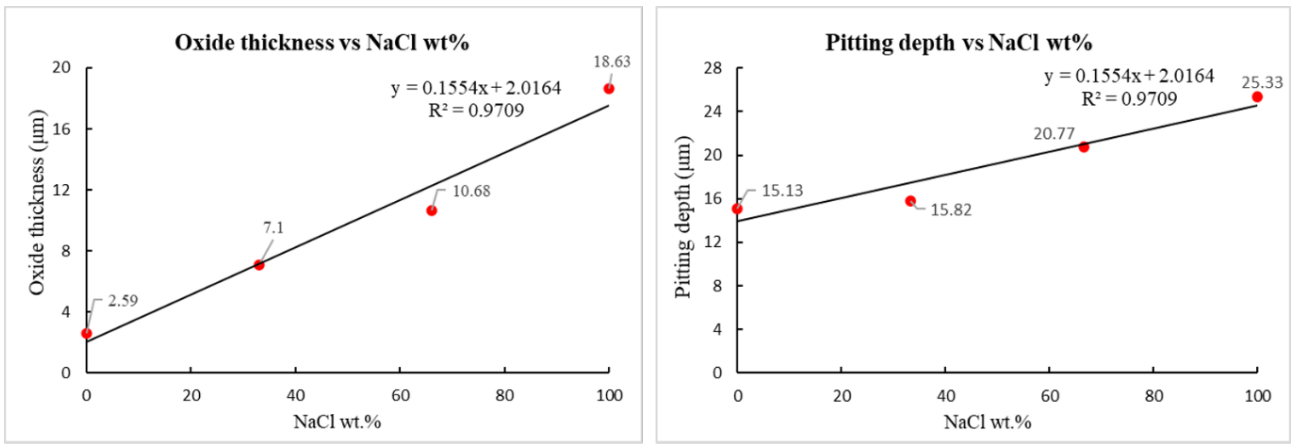

(a) (b)

Fig. 6. (a) Increase of oxide thickness relative to weight percentage of NaCl with hot corrosion treatment for 50 h; (b) Increase of pitting depth relative to weight percentage of NaCl with hot corrosion treatment for 50 h.

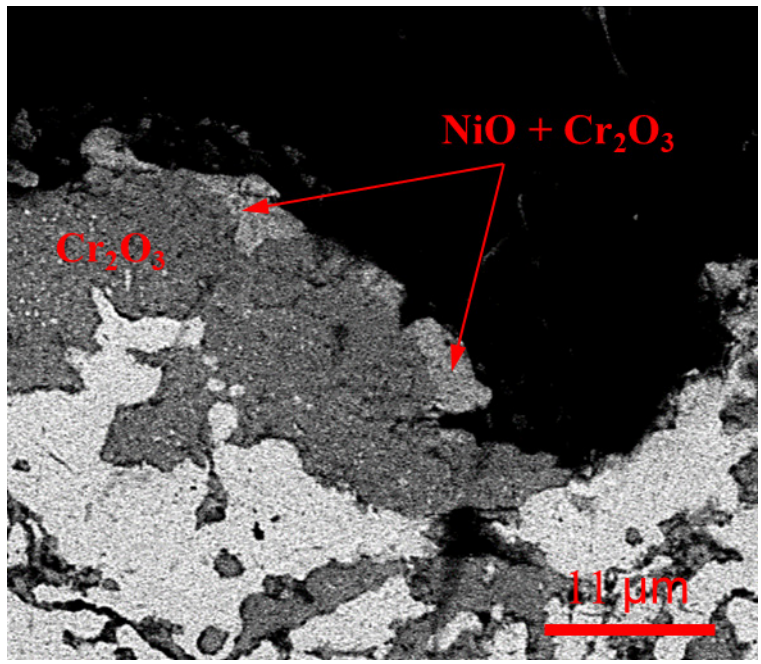

Fig. 7. Micrograph of oxide morphology Cr_2O_3 and NiO + Cr_2O_3 on specimen 50D.

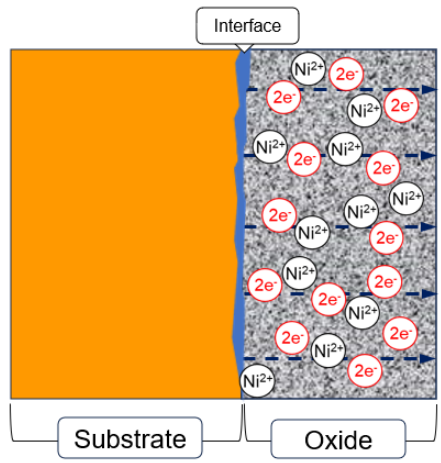

Fig. 8. Illustration of Cr depletion, oxidation of Ni-Cr, and formation of Cr_2O_3 and NiO.

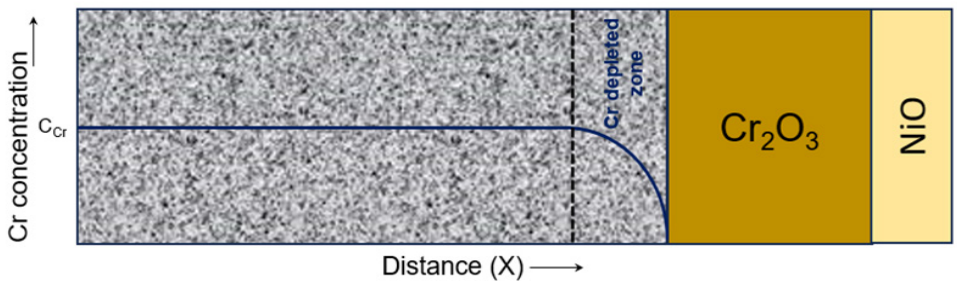

Fig. 9. Illustration of Ni oxidation.

whereas C atom diffused faster and reacted with oxygen to form the gases CO_2 and CO as in the reaction below [26]. The reactions are shown as Eq. (7) and Eq. (8).

$$C_{(s)} + O_{2(g)} = CO_{2(g)};\ \Delta G_{750}: -788.647\ kJ\ mol^{-1} \quad (7)$$
$$CO_{2(g)} + C_{(s)} = 2CO_{(g)};\ \Delta G_{750}: 240.024\ kJ\ mol^{-1} \quad (8)$$

Cr_3C_2 compound oxidized into Cr_2O_3 can be written as follows, Eq. (9).

$$Cr_3C_{2(s)} + 13/4O_{2(g)} = 3/2Cr_2O_{3(s)} + 2CO_{(g)};\ \Delta G_{750}: -3559.451\ kJ\ mol^{-1} \quad (9)$$

The XRD result showed that no spinel compound such as $NiCr_2O_4$ was formed. However, at higher temperatures (1000°C) spinel $NiCr_2O_4$ can potentially be formed. As stated in Eq. 10. Spinel $NiCr_2O_4$ may also be formed due to the advanced reaction between NiO and Cr_2O_3[27].

$$NiO + Cr_2O_3 = NiCr_2O_4;\ \Delta G_{750}: -32.785\ kJ\ mol^{-1} \quad (10)$$

Spalling of oxide layers

Spalling was evident on every specimen (50A, 50B, 50C and 50D), which can be seen from the SEM micrograph as displayed in Fig. 10a. Oxide spalling was mainly caused by two factors: the Pilling - Bedworth Ratio (PBR) of Cr_2O_3 was relatively high at 2.07, and the element Sulphur (S) and Cl_2 were segregated from the interface of the spalled oxide [28, 29]. The S element derived from salt $NaSO_4$ while the gas Cl_2 derived from NaCl. Back scattering element mapping showed that specimen 50A experienced oxide spalling, which is evidence that the oxide was Cr_2O_3 (Fig. 10b). On the other hand, the PBR value of NiO was 1.65 [28, 29]. The PBR value of $1 < PBR < 2$ is a passive oxide layer that provides a protective effect against further oxidation.

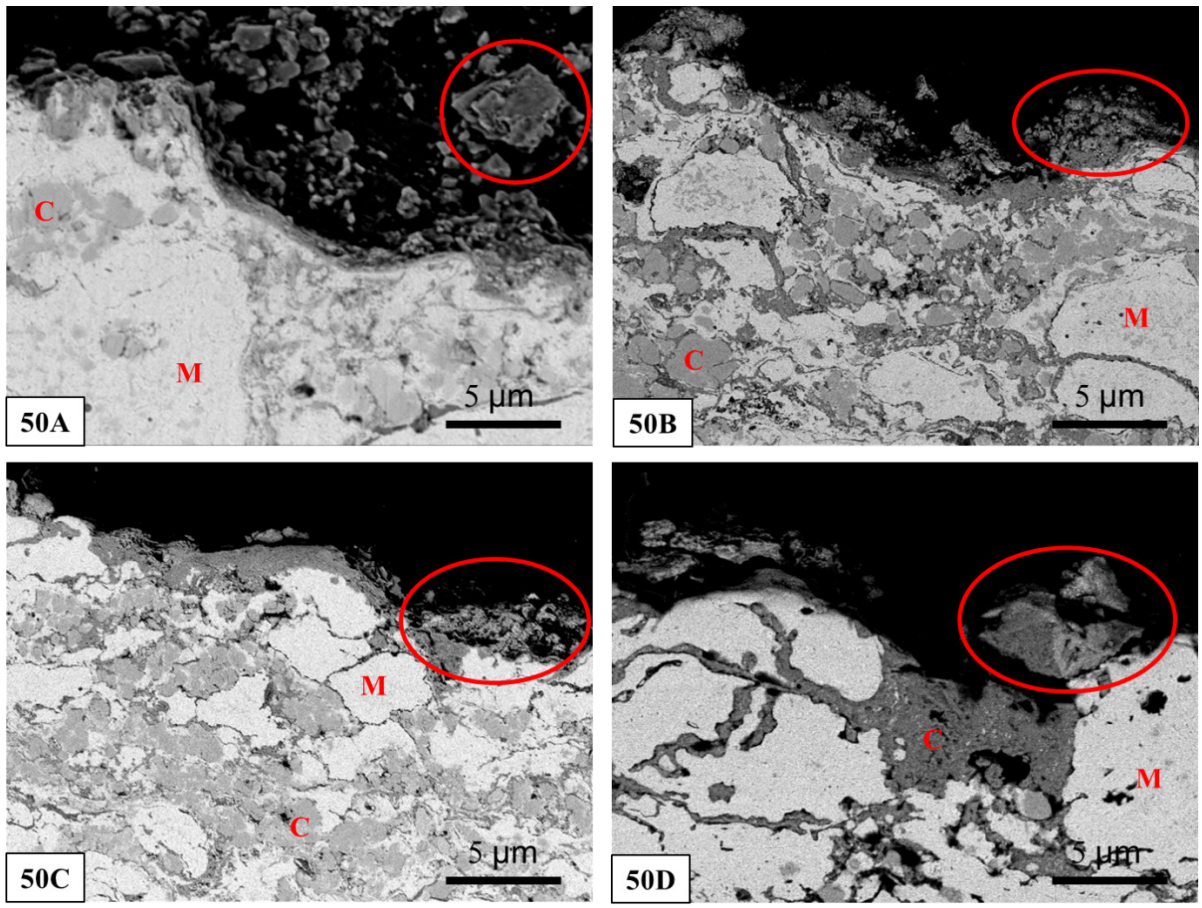

Fig. 10. Oxide spallation on every specimen 50A, 50B, 50C and 50D. Remarks, M = matrix; C = carbide.

CONCLUSIONS

From this series of experiments, it can be concluded that hot corrosion type II was evident in specimens with exposure to molten salt Na_2SO_4/NaCl (66/33, 33/66, 0/100), but it was not evident in specimens exposed to molten salt 100 % Na_2SO_4.The higher the NaCl concentration, the thicker the Cr_2O_3 oxide is formed. The deeper pitting on the surface of the specimen shows that more oxide NiO formed on the oxide Cr_2O_3 surfaces. A linear rise in the oxide thickness and depth of pitting was evident on the hot corrosion treated specimen for 50 h at a temperature of 750°C. Decarburization of Cr_3C_2 was evident in every specimen during the hot corrosion test and Cr was subsequently oxidized into Cr_2O_3.

Acknowledgments

The authors would like to thank all technicians and researchers who participated in this research work at Research Center for Advance Materials and Research Center for Smart Mechatronics of National Research and Innovation Agency (BRIN) Indonesia.

Authors' contributions

M.W., A.W.: experimental work and writing of a manuscript; M.M.: Review and editing of the manuscript; B.P., E.M.: Material and technological provision; E.J.: Facilitating thermal spray coating process.

REFERENCES

1. U. Nations, World Population Prospects 2024: Summary of Results, 2024.
2. U.S.E.I.A. Independent Statistics and Analysis, Electricity. 2025.
3. H. Ding, S. Ding, Q. Tan, C. Zhang, Q. Fang, T. Yang, Improving power ramp rate of a coal-fired power plant by a bypass steam accumulator, Heliyon., 10, 11, 2024, 32412.
4. A. Harutyunyan, K. Badyda, M. Wołowicz, Analyzing of different repowering methods on the example of 300 MW existing steam cycle power plant using gatecycle™ software, Energy., 314, 2025, 134228.
5. M. Baranda, C. Mayo, R. Diaz, R. Rodriguez, F.J. Pérez, Comparative environmental assessment of coated ferritic steels suited to steam turbines of coal-fired supercritical and ultra-supercritical power plants, J. Clean. Prod., 443, 2024, 141226.
6. R.C. Zeng, L. Sun, Y.F. Zheng, H.Z. Cui, E.H. Han, Corrosion and characterisation of dual phase Mg-Li-Ca alloy in Hank's solution: The influence of microstructural features, Corros Sci., 79, 2014, 69-82.
7. S. Medabalimi, A.M. Hebbale, S. Gudala, U. Rokkala, M.R. Ramesh, Studies on high temperature erosion behavior of HVOF-sprayed (Cr_3C_2-NiCr) Si and WC-Co/NiCrAlY composite coatings, Int J Refract Metals Hard Mater., 127, 2025, 106970.
8. M. Waldi, H.B. Samudra, A. Maulana, A. Leksana, D. Hadi Prajitno, H. Tjahaya, Cyclic oxidation behavior of HVOF thermally sprayed wc cermet based on AISI 1045 steel, MIPI J. Ind. Res. Innov., 16, 2, 2022, 73-80.
9. S. Singh, K. Goyal, R. Bhatia, A review on protection of boiler tube steels with thermal spray coatings from hot corrosion, Mater Today Proc., 56, 2022, 379-383.
10. S. Septianissa, B. Prawara, E.A. Basuki, E. Martides, E. Riyanto, Improving the hot corrosion resistance of γ/γ' in Fe-Ni superalloy coated with Cr_3C_2-20NiCr and NiCrAlY using HVOF thermal spray coating, Int. J. Electrochem. Sci., 17, 2022, 221231.
11. J. Lauzuardy, E.A. Basuki, E. Martides, S. Septianissa, B. Prawara, E. Juniarto, microstructure characteristics of Cr_3C_2-NiCr coatings deposited with the high-velocity oxy-fuel thermal-spray technique, Mater. Tehnol., 58, 2, 2024, 137-145.
12. M. Waldi, E.A. Basuki, B. Prawara, Quality characterization of HVOF thermal spray coating with NiCr matrix composite for protection application of coal fired boiler tubes, IOP Conf. Ser. Mater. Sci. Eng., 432, 2018, 012011.
13. S. Hong, Y. Wu, Q. Wang, G. Ying, G. Li, W. Gao, B. Wang, W Guo, Microstructure and cavitation-silt erosion behavior of high-velocity oxygen-fuel (HVOF) sprayed Cr_3C_2-NiCr coating, Surf. Coat. Technol., 225, 2013, 85-91.
14. H. Sun, H. Ding, T. Liu, Unveiling the effect of vacuum heat treatment on HVOF-sprayed high entropy cantor alloy coatings: microstructure, diffusion behavior and mechanical property, J. Mater. Res. Technol., 33, 2024, 9033-9043.
15. FactSage Software and Database, Binary phase

diagram of NaCl-Na_2SO_4, 2025.
16. C.C. Tsaur, J.C. Rock, C.J. Wang, Y.H. Su, The hot corrosion of 310 stainless steel with pre-coated NaCl/Na_2SO_4 mixtures at 750°C', Mater Chem Phys., 89, 2-3, 2005, 445-453.
17. D.J. Young, High Temperature Oxidation and Corrosion of Metals, Elsevier Ltd, 2016.
18. D.D. Warman, W.H. Evans, V.B. Parker, R.H. Schumm, I. Halow, S.M. Bailey, K.L. Churney, R.L. Nuttal, The NBS tables of chemical thermodynamic properties. Selected values for inorganic and C1 and C2 organic substances in SI units, J. Phys. Chem., 11, 2, 1982, 1-392.
19. N. Hiraide, T. Muneno, H. Kajimura, Reaction of Cr and Cr oxide with NaCl at elevated temperature, Zairyo-to-Kankyo., 58, 10, 2009, 348-355.
20. M.A. Uusitalo, P.M. J. Vuoristo, T.A. Mäntylä, High temperature corrosion of coatings and boiler steels in oxidizing chlorine-containing atmosphere, Mater. Sci. Eng., A, 346, 1-2, 2003, 168-177.
21. C.P. Bergmann, J. Vicenzi, Protection Against Erosive Wear Using Thermal Sprayed Cermet: A Review, Springer-Verlag Berlin Heidelberg, 2011.
22. A. Ganvir, N. Markocsan, S. Joshi, Influence of isothermal heat treatment on porosity and crystallite size in axial suspension plasma sprayed thermal barrier coatings for gas turbine applications, Coatings., 7, 1, 2017, 7010004.
23. F.S. Pettit, G.H. Meier, Oxidation and hot corrosion of superalloys, Superalloys., 85, 1, 1984, 651-687.
24. E. Epifano, D. Monceau, Ellingham diagram: A new look at an old tool, Corros. Sci., 217, 2023, 111113.
25. M. Roy, K.K. Ray, G. Sundararajan, Erosion-oxidation interaction in Ni and Ni-20Cr alloy, Metall Mater Trans A Phys Metall Mater Sci., 32, 6, 2001, 1431-1451.
26. B. Edenhofer, D. Joritz, M. Rink, K. Voges, in: E. J. Mittemeijer, M.A.J. Somers (Eds.), Thermochemical surface engineering of steels.
27. Y. Ding, T. Hussain, D.G. McCartney, High-temperature oxidation of HVOF thermally sprayed NiCr-Cr_3C_2 coatings: microstructure and kinetics, J. Mater. Sci., 50, 20, 2015, 6808-6821.
28. J.Y. Du, Y.L. Li, F.Y. Li, X.J. Ran, X.Y. Zhang, X.X. Qi, Research on the high temperature oxidation mechanism of Cr_3C_2-NiCrCoMo coating for surface remanufacturing, J. Mater. Res. Technol., 10, 2021, 565-579.
29. C. Xu, W. Gao, Pilling-Bedworth ratio for oxidation of alloys, Mat Res Innovat., 3, 4, 2000, 231-235.